ACS APPLIED MATERIALS & INTERFACES

www.acsami.org

Research Article

Remote Control of Neural Stem Cell Fate Using NIR-Responsive Photoswitching Upconversion Nanoparticle Constructs

Yixiao Zhang, Lisa M. Wiesholler, Hudifah Rabie, Pengfei Jiang, Jinping Lai, Thomas Hirsch, and Ki-Bum Lee*

Cite This: *ACS Appl. Mater. Interfaces* 2020, 12, 40031−40041

Read Online

ACCESS | Metrics & More | Article Recommendations | Supporting Information

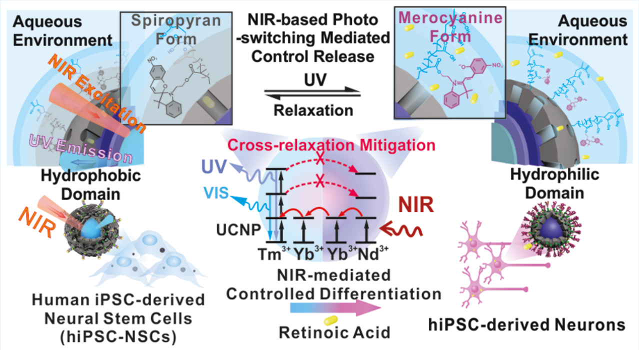

ABSTRACT: Light-mediated remote control of stem cell fate, such as proliferation, differentiation, and migration, can bring a significant impact on stem cell biology and regenerative medicine. Current UV/vis-mediated control approaches are limited in terms of nonspecific absorption, poor tissue penetration, and phototoxicity. Upconversion nanoparticle (UCNP)-based near-infrared (NIR)-mediated control systems have gained increasing attention for vast applications with minimal nonspecific absorption, good penetration depth, and minimal phototoxicity from NIR excitations. Specifically, 808 nm NIR-responsive upconversion nanomaterials have shown clear advantages for biomedical applications owing to diminished heating effects and better tissue penetration. Herein, a novel 808 nm NIR-mediated control method for stem cell differentiation has been developed using multishell UCNPs, which are optimized for upconverting 808 nm NIR light to UV emission. The locally generated UV emissions further toggle photoswitching polymer capping ligands to achieve spatiotemporally controlled small-molecule release. More specifically, with 808 nm NIR excitation, stem cell differentiation factors can be released to guide neural stem cell (NSC) differentiation in a highly controlled manner. Given the challenges in stem cell behavior control, the developed 808 nm NIR-responsive UCNP-based approach to control stem cell differentiation can represent a new tool for studying single-molecule roles in stem cell and developmental biology.

KEYWORDS: *upconversion nanoparticles, 808 nm NIR upconversion, NIR light-responsive control, stem cell differentiation, neurogenesis*

1. INTRODUCTION

Stem cell fate, function, and plasticity have known to be dynamically regulated in a spatiotemporally controlled manner by multiple cues, including biomolecules and physical signals.[1−3] Therefore, understanding the spatiotemporal functions of specific signals and further achieving precise control of stem cell behaviors in both spatially and temporally controlled manner would be essential for studying physiological mechanisms, identifying pathogenic pathways, and developing stem-cell-based treatments for devastating diseases.[4−6] For instance, neurogenesis is a complicated biological process in which several key behaviors of neural stem cells (NSCs), such as proliferation, differentiation, migration, axonal growth, and synapse formation, are heavily involved.[7−11] To investigate as well as further regulate the complex process of NSC neurogenesis, light, especially in the near-infrared (NIR) region, can be an ideal stimulus for probing and modulating the spatiotemporal dynamics of signals in living neural cells and neuronal networks.[12−14] In this regard, photoresponsive nanomaterials have gained increasing scientific interests in achieving cell behavior control attributed to their exceptional photophysical properties.[15−19] However, conventional photoresponsive nanomaterial-based biological manipulations are heavily dependent on ultraviolet and visible (UV−vis) light as the main excitation source, which is intrinsically limited by its phototoxicity and low penetration depth, owing to light scattering and absorption.[20−22] With recent developments in nanomaterials, lanthanide-based upconversion nanoparticles (UCNPs) have been developed with capabilities of generating UV/vis emissions from NIR excitations for applications in imaging,[23,24] photodynamic therapy,[25−27] immunotherapy,[28] drug delivery,[29−32] optogenetics,[33−35] and cell behavior manipulation.[18,36−40] Recently, neodymium (Nd) and ytterbium (Yb) co-sensitized UCNPs have been demonstrated to possess an 808 nm sensitization capability.[41] Consequently, they have attracted significant attention due to the minimized heating effect and enhanced tissue penetration depth (Figure

Received: June 3, 2020
Accepted: August 11, 2020
Published: August 11, 2020

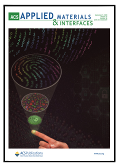

ACS Publications

https://dx.doi.org/10.1021/acsami.0c10145
ACS Appl. Mater. Interfaces 2020, 12, 40031−40041

Scheme 1. Scheme of Remotely Controlled Stem Cell Differentiation Using 808 nm Upconversion Nanoparticle Constructs[a]

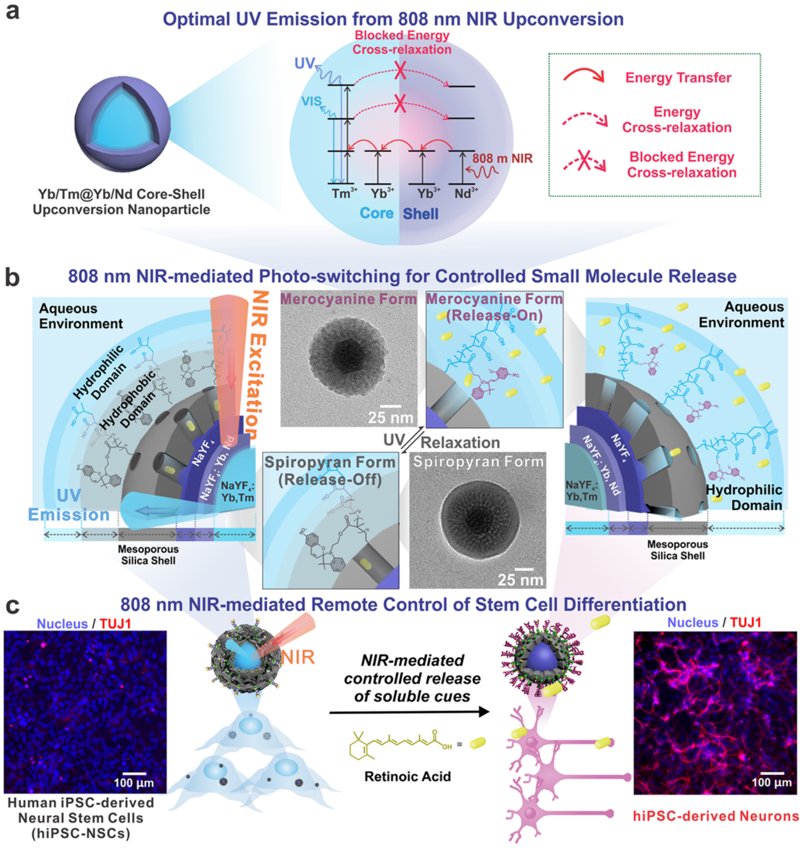

[a](a) Schematic diagram demonstrating the energy migration pathways in NaYF4:Yb/Tm@NaYF4:Yb/Nd-structured UCNPs. Cross-relaxation is mitigated (red arrows with cross) based on spatial separation of the Tm^{3+} and Nd^{3+}. (b) Schematic diagram of the 808 nm NIR-mediated photoswitching of the spiropyran polymer on the designed UCNP nanoconstructs (**UCNP@mSi@pSP**) to induce on-demand small-molecule release. (c) Proof-of-concept demonstration for 808 nm NIR-based neural stem cell differentiation using the aforementioned **UCNP@mSi@pSP** system.

S1).[42−45] Nevertheless, a major challenge for utilizing 808 nm UCNP systems for bioapplications falls on the detrimental cross-relaxation from activator dopants to the co-sensitizer (Nd^{3+}), leading to lower overall emission output as well as a lower UV emission ratio.[46] The strategy to overcome this limitation is to utilize the core−shell structure to separate the Nd^{3+} from the activators.[47,48] Though much efforts and improvements have been made in 808 nm UCNP systems[49,50] and related biomedical research fields,[51−53] a few studies were conducted on improving 808 nm NIR upconversion UV emission yields and the corresponding applications in NIR-mediated neural stem cell differentiation control.

To address the challenges mentioned above, herein, we developed core−shell−shell 808 nm-sensitized upconversion nanocarriers for advanced small-molecule delivery (Scheme 1.a) that can generate intense UV emissions to trigger the isomerization of a photoswitching capping system [poly-spiropyran (**pSP**) moieties] (Scheme 1.b), which can be utilized to control the neuronal differentiation of stem cells in a remotely controlled manner (Scheme 1.c). More specifically, our unique 808 nm UCNP constructs were designed and synthesized with a multishell structure for minimizing cross-relaxation and a composition optimizing 808 nm NIR to UV upconversion (Scheme 1.a). Subsequently, this UCNP construct was modified with a mesoporous silica shell (**UCNP@mSi**) to be applied as a reservoir of small molecules and further functionalized with a photoresponsive polymeric shell containing spiropyran groups (**UCNP@mSi@pSP**) (Scheme 1.b). In conjunction with the **UCNP@mSi@pSP** system, a neurogenic differentiation factor named retinoic acid (RA), which is known to be highly involved in many developmental processes including neurogenesis of stem cells,[54,55] was delivered to human-induced pluripotent stem cell-derived neural stem cells (hiPSC-NSCs) to promote neuronal differentiation in a remotely controlled manner (Scheme 1.c). Consequently, the developed UV-emitting UCNPs could provide guiding information for designing and synthesizing 808 nm NIR-based nanodevices for various applications. Moreover, while we used RA as a proof-of-concept small molecule for neuronal differentiation, other differentiation factors can be easily incorporated into the **UCNP@mSi@pSP** platform to regulate a broad range of stem cell differentiation and lineage commitments. Thus, our novel 808 nm NIR-mediated method to control stem cell fate can be expanded to a variety of potential applications in stem cell therapy, neuroscience, and regenerative medicine.

2. RESULTS AND DISCUSSION

2.1. Developing 808 nm NIR-Mediated Photoswitching UCNP Constructs Based on UV Emission Optimization in Core−Shell-Structured UCNPs. To utilize 808 nm NIR as an excitation source for photoswitching of the **pSP**

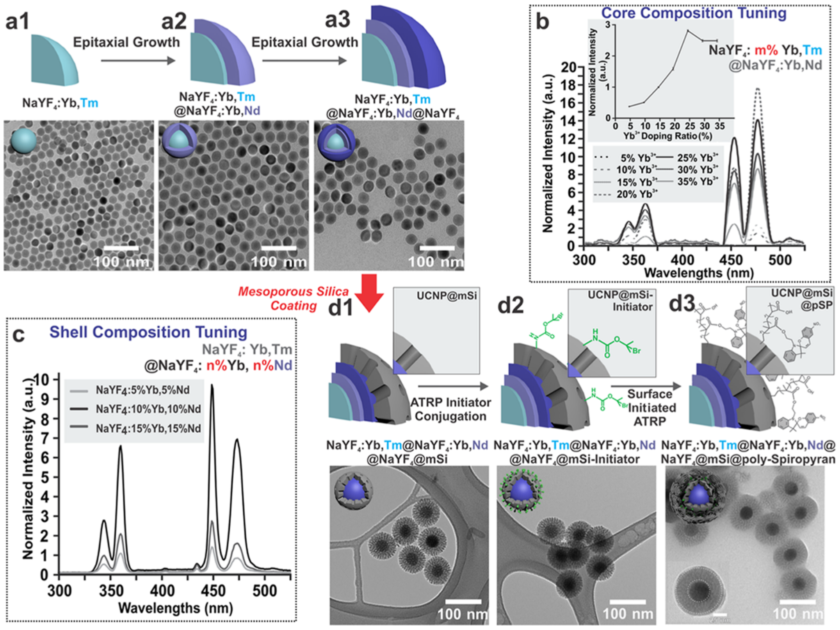

Figure 1. Synthesis and characterization of the core−shell−shell UCNP constructs for optimal UV emissions and photoswitching capability. (a) Schematic diagrams and transmission electron microscopy (TEM) characterization showing size and morphology evolution of the $NaYF_4$:Yb,Tm@$NaYF_4$:Yb,Nd@$NaYF_4$ core−shell−shell-structured UCNPs from core UCNPs $NaYF_4$:Yb,Tm (a1) to core−shell UCNPs $NaYF_4$:Yb,Tm@$NaYF_4$:Yb,Nd (a2) and to core−shell−shell UCNPs $NaYF_4$:Yb,Tm@$NaYF_4$:Yb,Nd@$NaYF_4$ (a3). (b) Upconversion luminescence (UCL) comparison of different sensitizer (Yb^{3+}) concentrations in the core (0−35%) with a doping ratio of 25% Yb^{3+} and 0.3% Tm^{3+} demonstrating the highest UV emission output from 808 nm excitation; inset: quantitative comparison of UV emission (368 nm) peak intensity of different Yb^{3+} concentrations. (c) Upconversion luminescence comparison of different co-sensitizers' (Nd^{3+} and Yb^{3+}) concentrations in the sensitizing shell where a doping ratio of 10% Yb^{3+} and 10% Nd^{3+} shows the optimal UV upconversion enhancement. (d) Schematc diagrams and TEM characterization showing the subsequent surface coatings: $NaYF_4$:Yb,Tm@$NaYF_4$:Yb,Nd@$NaYF_4$@mSi (UCNP@mSi) (d1), atom transfer radical polymerization (ATRP) initiator functionalization $NaYF_4$:Yb,Tm@$NaYF_4$:Yb,Nd@$NaYF_4$@mSi@Initiator (UCNP@mSi-initiator, initiator structures indicated in green) (d2), and surface-initiated ATRP of photoswitching polymer: $NaYF_4$:Yb,Tm@$NaYF_4$:Yb,Nd@$NaYF_4$@mSi@Initiator@pSP (**UCNP@mSi@pSP**, **pSP** structures indicated in gray) (d3) (insets: scale bar: 25 nm).

capping system, efficient NIR to UV/vis upconversion is an essential prerequisite. We achieved this goal by designing and synthesizing core−shell−shell UCNPs possessing: (1) tandem sensitization from Nd^{3+}/Yb^{3+} to Yb^{3+}/Tm^{3+} dopants and (2) cross-relaxation mitigation by spatial separation of Tm^{3+} and Nd^{3+} into the nanoparticle core and shell, respectively (Scheme 1.a).[20,21] $NaYF_4$ was selected as a host material due to its low lattice phonon energy of 350 cm^{-1}.[56] The core−shell−shell design consists of a $NaYF_4$:Yb/Tm core (Figure 1a1) and two outer shells with different functions. The first shell ($NaYF_4$:Yb/Nd) serves as an 808 nm NIR-absorbing layer (Figure 1a2), and the second shell serves as an inert coating ($NaYF_4$) that protects against surface quenching (Figure 1a3). Core−shell UCNPs ($NaYF_4$:*m*%Yb,0.3%Tm@$NaYF_4$:10%Nd,10%Yb) with variations in core Yb^{3+} doping ratio from 5 to 35% with a fixed shell composition ($NaYF_4$:10%Nd,10%Yb) were synthesized and optimized for efficient UV upconversion (Figure S2). Detailed luminescence characterization regarding size and doping ratio of the core and shells was performed to acquire the best efficiency for UV emissions, which are critical for triggering the release of the small molecule in the following studies. As a result, the highest emissions at 345 nm ($^1I_6 \rightarrow {}^3F_4$ transition) and 368 nm ($^1D_2 \rightarrow {}^3H_6$ transition) were obtained from a doping ratio of 25% Yb^{3+} and 0.3% Tm^{3+} in the core according to luminescence (Figure 1b) and lifetime measurements (Figure S3). Subsequently, we optimized the sensitizing shell composition by investigating variations in the doping ratio of Yb^{3+} (5−15%) and Nd^{3+} (5−15%), revealing that 10% Yb^{3+} and 10% Nd^{3+} showed optimal UV upconversion efficiency (Figures 1c and S4).

A second shell was grown on the optimized core−shell UCNPs ($NaYF_4$:25%Yb,0.3%Tm@$NaYF_4$:10%Nd, 10%Yb) to reduce surface defect-based quenching, showing an additional 33% increase of the upconversion emission at 368 nm, as can be observed in Figure S5. As a result, core−shell−shell UCNPs ($NaYF_4$:25%Yb,0.3%Tm@$NaYF_4$:10%Nd,10%Yb@$NaYF_4$) with optimal 808 nm-mediated UV emissions were obtained. The developed 808 nm sensitizing core−shell−shell UCNPs showed efficient UV emissions, resulting in a peak ratio (I_{368nm}/I_{475nm}) of 0.53 under 15 mW/cm^2 NIR illumination. The monodispersity of each nanoparticle structure through the synthetic steps of the core−shell−shell UCNPs was verified through transmission electron microscopy (TEM) (Figure S6a,b) as well as dynamic light scattering (DLS) characterizations (Figure S6c). The crystallinity of each synthetic step was confirmed by X-ray diffraction (XRD) measurements to show a β-hexagonal phase (Figure S6d). According to the TEM analysis, the final core−shell−shell UCNPs' dimensional information is summarized in Table S1. Moreover, the optimized nanoparticle composition was determined to be $NaYF_4$:24.5%Yb,0.27%Tm@$NaYF_4$:9.9%Nd,10.5%Yb@$NaYF_4$ through calculations and measurements using inductively coupled plasma optical emission spectrometry (Table S1).

Upon construction of the efficient 808-to-UV UCNPs, mesoporous silica (**mSi**) layer was further coated on the designed UCNPs to efficiently deliver the neurogenic factor (RA), as demonstrated in Figure 1d1. With the mesoporous

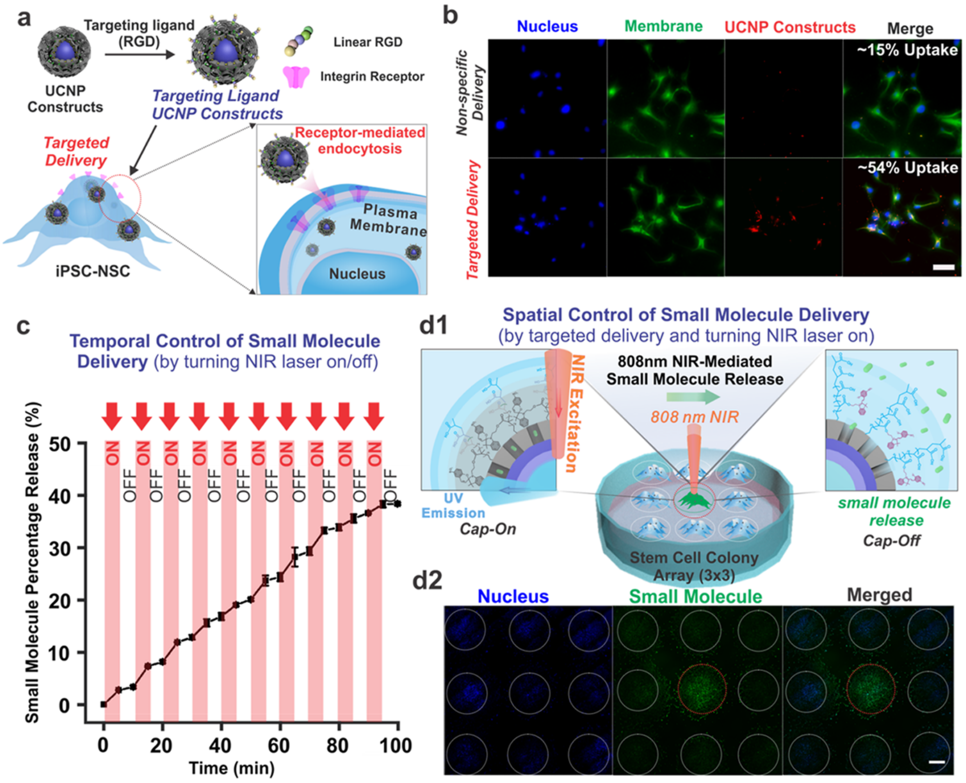

Figure 2. Receptor-mediated intracellular localization of UCNP@mSi@pSP and spatiotemporal control of small-molecule release. (a) Schematic illustration of the receptor-mediated uptake process of the UCNP constructs (**UCNP@mSi@pSP**). (b) Fluorescence microscopy images of live hiPSC-NSCs stained with DiO (membrane: green) and NucBlue (nucleus: blue) after 24 h incubation with RGD-modified **UCNP@mSi@pSP** (targeted delivery) and **UCNP@mSi@pSP** (nonspecific delivery) (scale bar: 50 μm). (c) Small-molecule release profile of the 808 nm NIR-mediated controlled release of fluorescein as model small molecule. An "on−off" release pattern can be observed, demonstrating the temporal control ability. (d) Spatial control of small-molecule release. (d1) Schematic diagram showing spatial control of small-molecule release in neural stem cell colony culture. (d2) Fluorescence microscopy characterization of fluorescein spatial controlled release in live hiPSC-NSCs colony culture. Note that the red circles indicate selective release of fluorescein in the center stem cell colony (scale bar: 1000 μm).

silica coating, the nanoparticle diameter reaches up to 83.7 ± 3.9 nm. To synthesize the **pSP**-based shell, a photoresponsive monomer spiropyran methacrylate (SPMA) was prepared and confirmed through ^{1}H NMR (Figure S7). The **pSP** polymer shell containing spiropyran-based moieties was formed on the mesoporous silica shell (**UCNP@mSi**) through surface-initiated atom transfer radical polymerization (ATRP). Due to the existence of active initiator sites on the **pSP**, a colloidal stabilizing polymer layer (polyacrylic acid) was further grafted onto the spiropyran polymer-coated UCNPs. The resulting nanoparticles were characterized by TEM (Figure 1d) and Fourier transform infrared (FTIR) spectroscopy (Figure S8). Thus, with the polymer coating, the final **UCNP@mSi@pSP** nanoparticle constructs possess a diameter of 96.1 ± 6.6 nm under TEM (Figure 1d3) and a hydrodynamic size of 144 nm (polydispersity index = 0.204) determined by the dynamic light scattering (DLS) analysis.

2.2. Demonstrating Spatiotemporally Controlled Release of Small Molecules Using 808 nm NIR-Mediated Photoswitching UCNP@mSi@pSP. Next, the synthesized **UCNP@mSi@pSP** was loaded with RA and transfected into hiPSC-NSCs to assess the nanoparticle's cellular uptake efficiency and its ability to deliver the neurogenic factor (RA) in a remotely controlled manner. To improve the cellular uptake efficiency, Arg-Gly-Asp (RGD) peptides were conjugated onto the surface of **UCNP@mSi@pSP**, promoting transfection via RGD-mediated integrin binding to the cellular membrane receptors (e.g., $\alpha_V\beta_3$ and $\alpha_V\beta_5$), which further facilitates receptor-mediated endocytosis[57] (Figure 2a). $\alpha_V\beta_3$ and $\alpha_V\beta_5$ integrin subunits, which are well-known RGD binding receptors,[57] are highly expressed during the neurogenic developmental process (neural tube).[58,59] As shown in Figure 2b, upconversion luminescence (UCL) and fluorescence microscopy images demonstrated that targeting ligand UCNP constructs' (RGD-modified **UCNP@mSi@pSP**) upconversion emissions (red) significantly overlapped with the hiPSC-NSCs' cytoplasm (green), compared to nonspecific UCNP constructs (non-RGD-modified **UCNP@mSi@pSP**), where little overlap could be observed. Furthermore, quantification of the percentage of hiPSC-NSCs with UCL positive signal (Figure S9) supported our hypothesis that RGD-modified **UCNP@mSi@pSP** demonstrated significantly more efficient cellular uptake (~54%) compared to non-RGD-modified constructs (~15%).

Meanwhile, the cell viability under 808 nm laser irradiation and transfection conditions were fully characterized for subsequent NIR-mediated neuronal differentiation experiments. A decreasing trend in hiPSC-NSC's viability was observed as the power density of the 808 nm laser increased (Figure S10a). For the NIR-mediated differentiation experimental conditions, a low power density (allowing for 90.75% cell viability) of 1.05 W/cm^2 was chosen. Minimal cytotoxicity was also observed from the nanoparticle constructs for concentrations up to 100 μg/mL (Figure S10b). In addition,

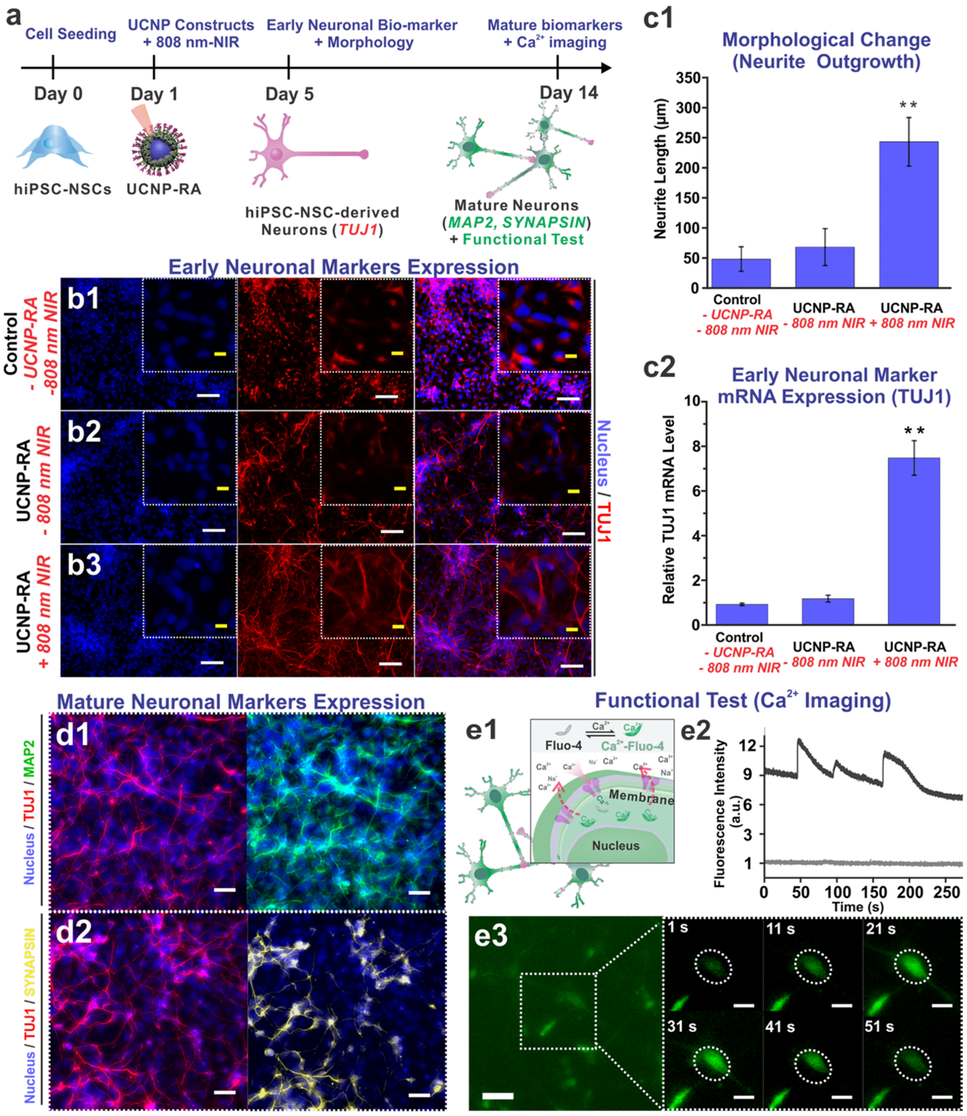

Figure 3. 808 nm NIR-mediated control of hiPSC-NSC's neuronal differentiation and maturation. (a) Schematic timeline of the 808 nm NIR-mediated in vitro differentiation control of hiPSC-NSCs. (b) Immunohistochemistry fluorescence microscopy images of hiPSC-NSCs stained against key neuronal marker (*TUJ1*: red fluorescence) in control group (b1), the UCNP-RA (**UCNP@mSi@pSP** loaded with retinoic acid) group (b2), and the UCNP-RA (**UCNP@mSi@pSP** loaded with RA) + 808 nm NIR group (b3) (scale bar = 100 μm; inset scale bar = 25 μm). (c) NIR-mediated hiPSC-NSCs neuronal differentiation characterization. (c1) Quantitative comparison of the morphological changes (neurite growth) of the aforementioned three treatment groups. (c2) Gene expression analysis using qPCR quantifying the *TUJ1* mRNA expression levels in hiPSC-NSCs in the three groups. (d) NIR-mediated differentiated neurons (ND neurons)' maturation marker characterization. (d1) Immunohistochemistry fluorescence microscopy characterization of the 808 nm ND neurons stained against key late neuronal marker MAP2 (green fluorescence) along with *TUJ1* staining (red fluorescence) (scale bar = 50 μm). (d2) Immunohistochemistry fluorescence microscopy characterization of the ND neurons staining against key synaptogenesis marker Synapsin (yellow fluorescence) along with *TUJ1* staining (red fluorescence) (scale bar = 50 μm). (e) ND neurons' functional test. (e1) Schematic diagram of Ca^{2+} imaging for characterizing ND neurons' functionality. (e2) Time traces for the fluorescence intensity change indicating spontaneous calcium ion influx from an active neuron (dark gray line) and an inactive neuron (light gray line). (e3) Fluorescence microscope image of 808 nm ND neurons stained with a commercially available calcium indicator dye: Fluo-4 (scale bar = 25 μm). Inset: spontaneous calcium fluctuations visualized by Fluo-4 fluorescence (green) for an active neuron (white circle) (scale bar = 20 μm) (error bars represent mean ± standard deviation (SD); $n = 3$, $*p < 0.05$, by one-way analysis of variance (ANOVA) with Tukey post hoc test).

the **UCNP@mSi@pSP** constructs showed minimal interference with cellular proliferation (Figures S11 and S12) as well as pluripotency (Figure S13). The desired remotely controlled release capability was demonstrated using fluorescein as a model molecule. A temporally controlled "on/off" release profile was demonstrated in Figure 2c, using the designed **UCNP@mSi@pSP**, triggered via 808 nm light. Specifically, an average of 4% of payload release was achieved within 5 min × 808 nm NIR illumination (1.05 W/cm^2), due to hydrophilic merocyanine generation from in situ UV emissions. The merocyanine form reverts to the spiropyran form once the 808 nm excitation is removed, reforming a hydrophobic layer that blocks the release of small molecules, as shown in Figure 2d1. Minimal release (7.18%) was observed under dark conditions after 8 h incubation, demonstrating the robustness of the photoswitching polymer-based capping system (Figure S14). The **UCNP@mSi@pSP**'s ability to release small molecules spatially in response to 808 nm NIR stimulation has also been demonstrated within a 3 × 3 colony array of hiPSC-NSCs, constructed using a poly(dimethylsiloxane) (PDMS) mold, as shown in Figure 2d2. The small molecule was locally released in the central colony where 808 nm NIR excitation was applied, as can be seen from the green fluorescence signal emanating from the irradiated colony (Figure S15). To further corroborate the photoswitching-based spatial release mechanism, temperature fluctuation was monitored, showing negligible media temperature difference under 808 nm (1.05 W/cm^2) illumination compared to control condition (0 W/cm^2) (Figure S16a,b). It is noteworthy that, under the same power density (1.05 W/cm^2), 980 nm illumination showed a significant media temperature fluctuation and a 7.8 K increase in bulk media temperature after 5 min 980 nm NIR treatment, further demonstrating the advantages of 808 nm NIR with minimized heating effect (Figure S16b) and enhanced tissue penetration (Figure S16d). These results showcased the **UCNP@mSi@pSP**-mediated small-molecule-releasing capability under 808 nm excitation within a two-dimensional (2D) neural stem cell network in a spatiotemporally controlled manner.

2.3. Investigating 808 nm NIR-Controlled hiPSC-NSCs Neuronal Differentiation Using Neurogenic Factor-Loaded UCNP@mSi@pSP. Recent advances in stem cell biology hold great potentials for developing new approaches for the treatment of many devastating neurodegenerative diseases and genetic disorders. Stem-cell-based therapies for regenerating functional neurons and restoring neuronal functions to damaged CNS areas can be beneficial for realizing stem cell therapy for such diseases. These approaches inevitably require the robust generation of engraftable cell sources of functional neural cells and better control of stem cell neuronal differentiation in a controlled and safe manner.[60,61] Thus, upon the construction of the small-molecule delivery system, we evaluated the ability for the remotely controlled release of RA (a small-molecule neurogenic factor) under 808 nm excitation to induce neuronal differentiation of hiPSC-NSCs.

As explained in Figure 3a, hiPSC-NSCs were seeded and treated with RGD-modified **UCNP@mSi@pSP** containing RA molecules followed by 808 nm light exposure (1.05 W/cm^2) for 15 min (5 min exposure intervals) prior to further culturing and characterization assays. After 5 days of stem cell culture, immunohistochemistry and quantitative polymerase chain reaction (qPCR) analytical methods were performed to evaluate the hiPSC-NSCs neuronal differentiation. Interestingly, the control group (Figure 3b1) and the nanoparticle-construct-treated group (UCNP-RA) (Figure 3b2) present a significantly lower expression of an early neuronal marker, neuron-specific class III β-tubulin (*TUJ1*), compared to the group treated with 808 nm NIR and the UCNP constructs (UCNP-RA + 808 nm NIR) (Figure 3b3). Furthermore, a dramatic neuronal morphological change was observed in the "UCNP-RA + 808 nm NIR" group compared to the control and "UCNP-RA" groups, demonstrating a typical neurite outgrowth morphology, indicating neuronal lineage commitment (Figure 3b).[62] Such neuronal morphological change was quantified by measuring neurite length according to the *TUJ1* immunohistochemistry staining, with the UCNP-RA + 808 nm NIR group showing significantly increased quantity and length of neurite outgrowths compared to the control and UCNP-RA groups (Figure 3c1). Furthermore, this controlled neurogenesis was corroborated with *TUJ1* mRNA expression level characterization through qPCR (Figure 3c2), with a sevenfold *TUJ1* upregulation in the UCNP-RA + 808 nm NIR group compared to the control group. As a result, the neuronal differentiation from human neural stem cells (hiPSC-NSCs) was successfully controlled using the **UCNP@mSi@pSP** system in an NIR-mediated manner.

2.4. Confirming Maturation and Functionality of the hiPSC-NSC-Derived Neurons. To further evaluate the maturity and functionality of the differentiated neurons from hiPSC-NSCs, the experimental group was maintained under differentiation conditions for up to 14 days to characterize mature neuronal markers and functional activities. As shown in Figure 3d1,d2, the immunohistochemistry results showed that the **UCNP@mSi@pSP**-based RA delivery system was a robust and effective method for the induction of mature neuronal differentiation in hiPSC-NSCs. Specifically, neuron-specific microtubule-associated protein 2 (*MAP2*), which is associated with nerve functions as well as neuronal cell structures,[63] was found highly expressed in the differentiated neurons (Figure 3d1). Moreover, as an indicator of mature neuronal network synaptogenesis,[64] Synapsin was selected and found highly expressed in the differentiated neurons, as can be seen in Figure 3d2. To characterize the functionality of differentiated neurons, we performed calcium imaging to test their response to potential differences (Figure 3e). Functionally active neurons spontaneously fire action potentials allowing influx of cations including calcium ions (Figure 3e1).[65] Using a calcium indicator (Fluo-4), corresponding intracellular calcium ion fluctuations were monitored. Furthermore, the fluorescence changes were quantified (Figure 3e2) and observed (Figure 3e3) for spontaneous fluctuations of calcium ions in neurons over 250 s, while the inactive control neurons showed minimal fluorescence intensity changes. A recent study has shown that low-power blue illumination generated from UCNPs can activate the melanopsin/TRPC6 pathway and promote NSC differentiation into glial cells instead of neurons in a nongenetic manner.[66] This finding further necessitates our **UCNP@mSi@pSP**-based approach for NIR-mediated NSC differentiation into functional neurons.

3. CONCLUSIONS

In summary, this work demonstrated an 808 nm NIR-mediated photoswitching upconversion nanosystem (**UCNP@mSi@pSP**) for remote control of stem cell fate. The unique core−shell−shell-structured UCNP design and synthesis enabled us to improve the UV upconversion luminescence significantly, which can complement recent advances in the principle, design, and synthesis of NIR photonic nanomaterials with various bioapplications. Furthermore, the spiropyran-based gatekeeping system allows us to release small-molecule drugs in a controlled manner. Particularly, the application of NIR-mediated nanoparticle constructs to modulate the targeted key signaling pathways in stem cells would be beneficial not only for selective stem cell fate control but also for dissecting signaling cascades affected by other stem cell microenvironments such as cell−cell interactions and biophysical/mechanical cues in vitro and potentially in vivo. Collectively, our new strategy and demonstration for the 808 nm NIR-mediated remote control of stem cell differentiation using the UCNP nanoparticle constructs (**UCNP@mSi@pSP**) can benefit future advancement of nanotechnology, stem cell biology, drug delivery, and neuroregenerative medicine.

4. METHODS

4.1. Materials. Lanthanide chloride hexahydrates (>99.9%) were purchased from Sigma-Aldrich and Treibacher Industrie AG. Oleic acid and 1-octadecene (both technical grade, 90%) were obtained from Alfa Aesar. Ammonium fluoride, 2-bromoisobutyryl bromide (BiBB), CuCl, dimethyl sulfoxide (DMSO), dichloromethane (DCM), methanol, *N*,*N*-dimethylformamide (DMF), tetraethyl orthosilicate (TEOS), (3-aminopropyl)triethoxysilane (APTES), *N*-cetyltrimethylammonium bromide (CTAB), paraformaldehyde, 1,1,4,7,10,10-hexamethyltriethylenetetramine (HMTETA), sodium hydroxide (NaOH), methanol, methacryloyl chloride, *tert*-butyl acrylate (*t*BA), tetrahydrofuran (THF, anhydrous), trifluoroacetic acid (TFA), *N*-hydroxysuccinimide (NHS), *N*-(3-dimethylaminopropyl)-*N*′-ethylcarbodiimide hydrochloride (EDC·HCl), hemoglobin (human), and intralipid were purchased from Sigma-Aldrich. Chloroform, ethyl acetate, sodium azide, and gelatin were purchased from Fisher Scientific. Ethanol (200 proof) was purchased from Decon Laboratories. 1-(2-Hydroxyethyl)-3,3-dimethyl-6-nitrospiro-(2*H*-1-benzopyran-2,2-indoline) (SP-OH) was purchased from TCI America. Sylgard 184 was purchased from Ellsworth Adhesive. All chemicals were used as received, without any further purification. Solvents for NMR analysis (Cambridge Isotope Laboratories) were used as received.

4.2. Characterizations. Transmission electron microscopy (TEM) was implemented with a 120 kV Philips CM12 (www.fei.com) microscope. A Malvern Zetasizer was used for dynamic light scattering (DLS). X-ray powder diffraction (XRD) patterns with a resolution of 0.005° (2θ) were collected using a Huber Guinier G670 diffractometer (www.xhuber.com) with a Cu source (Kα radiation, λ = 1.54060 Å) operating at 40 kV and 30 mA. For the determination of the composition and concentration of the UCNPs, a flame-EOP inductively coupled plasma optical emission spectrometer (ICP-OES) from Spectro (www.spectro.com) was used. Luminescence spectra of UCNPs were measured with an Aminco Bowman Series 2 luminescence spectrometer (Thermo Electron Corporation). The spectrometer was equipped with an external continuous wave (CW) 808 nm laser module (200 mW, ∼15 mW/cm^2), obtained from Picotronic. The luminescence lifetime was measured by a homemade lifetime measurement setup consisting of an 808 nm laser CW laser module (200 mW, ∼15 mW/cm^2), an optical chopper, a temperature-controlled cuvette holder with integrated magnetic stirrer, and a collection lens filter wheel and mount for optical fiber. UV−vis absorption spectra were recorded on a Varian Cary 50 spectrophotometer. Fluorescence spectra were recorded on a Varian Cary Eclipse fluorescence spectrophotometer with external NIR lasers with wavelength of 808 or 980 nm as an excitation light source (CNI high-power fiber-coupled diode laser system, FC-W-980, and FC-W-808). The total output powers for the lasers are tunable from 1 mW to 10 W. The power density was detected by a 1916-R handheld optical power meter with a thermophile detector (purchased from Newport Corporation). Unless otherwise stated, all spectra were obtained from the hexane dispersion of nanoparticles (1 wt %). ^{1}H NMR was acquired on Varian 300 MHz NMR spectrometer.

4.3. Synthesis of NaYF$_4$:*m*%Yb,0.3%Tm. The synthesis of Ln^{3+}-doped NaYF$_4$ nanocrystals was performed by a modified procedure based on a protocol reported by Wilhelm et al.[67] For the synthesis of 1 mmol β-NaYF$_4$:*m*%Yb,0.3%Tm particles with a specific dopants molar ratio, the corresponding molar ratios of the lanthanide chlorides were dissolved in methanol (5 mL) and transferred into a 50 mL three-neck round-bottom flask. Under nitrogen flow, oleic acid (8 mL) and 1-octadecene (15 mL) were added into the flask. This solution was then heated to 160 °C and put under vacuum for 30 min to obtain a clear solution. The solution was cooled down to room temperature. Subsequently, a 10 mL methanol solution of 4.0 mmol NH$_4$F and 2.5 mmol NaOH was added into the flask, and the suspension was kept at 120 °C for 30 min before heating to reflux (ca. 320 °C). The heating time was controlled by the appearance of upconversion luminescence from the synthesis flask via illumination with a 980 nm CW laser (200 mW). As soon as the upconversion luminescence can be identified by the bare eye, the solution was kept at reflux for an additional 8 min. To obtain the full transformation of the nanocrystals from the α-phase to the β-phase, a heating time of 15 min was adopted. The particles were precipitated by the addition of an excess of ethanol and collected by centrifugation at 1000*g* for 5 min. The precipitate was washed with chloroform/ethanol (1:10 v/v) two times and five times with cyclohexane/acetone (1:10 v/v) by repeated redispersion−precipitation−centrifugation cycles. In the end, for removing aggregates, the particles were dispersed in 10 mL cyclohexane, centrifuged at 1000*g* for 3 min, and the supernatant was collected.

4.4. Synthesis of Core−Shell NaYF$_4$:*m*%Yb,0.3%Tm@NaYF$_4$:*n*%Yb,*n*%Nd and NaYF$_4$:*m*%Yb,0.3%Tm@NaYF$_4$:*n*%Yb,*n*%Nd@NaYF$_4$. Synthesis of shell precursor material α-NaYF$_4$:*n*%Yb,*n*%Nd is similar to the synthesis of β-NaYF$_4$:*m*%Yb,0.3%Tm particles except for the composition of the lanthanide chlorides and the last heating step under reflux (320 °C). Here, the solution was kept at 240 °C for 30 min to obtain the cubic lattice nanocrystals. The synthesized shell precursors were collected following similar procedures to those described above. The coating method was adopted from the previous report with modifications.[68] The as-synthesized core UCNP β-NaYF$_4$:*m*%Yb,0.3%Tm was transferred into a 50 mL three-neck round-bottom flask under N$_2$. For 1 mmol total content of UCNP core particles, 5 mL of oleic acid and 5 mL of 1-octadecene were added. The flask was heated to 100 °C under vacuum for 1 h to obtain a clear solution. After this, the β-NaYF$_4$ particles were heated to reflux at 320 °C. The shell precursor α-NaYF$_4$:*n*%Yb,*n*%Nd was dispersed into 1 mL of oleic acid/1-octadecene mixture (1:2 v/v). The shell precursor was quickly injected into the reaction flask. The reaction temperature decreased to ∼300 °C. The solution was kept for another 10 min at reflux. Then, the solution was cooled down to room temperature. The same protocol was used for growing a second inert shell of NaYF$_4$ around the β-NaYF$_4$:25%Yb,0.3%Tm@NaYF$_4$:10%Yb,10%Nd particles. The precipitation and purification of the synthesized nanoparticles were performed as described above.

4.5. Mesoporous Silica Shell Coating. The synthesis of mesoporous silica-coated upconversion nanoparticles was conducted based on a procedure modified from our previous protocol.[30] The synthesized NaYF$_4$:25%Yb,0.3%Tm@NaYF$_4$:10%Yb,10%Nd@NaYF$_4$ (15 mg) in cyclohexane (600 μL) was mixed with a CTAB solution (25 mL, 500 mg). The mixture solution was sonicated for 30 min by a probe sonicator, resulting in a transparent solution. Thereafter, the mixture solution was transferred to a dry 100 mL round-bottom flask with an addition of 150 μL of a 2 M NaOH aqueous solution. The mixture was stirred at 60 °C for 30 min, followed by 50 μL of TEOS added to 1.5 mL of ethyl acetate in a dropwise manner. The mixture was further stirred at 60 °C for 24 h. Further, amine group functionalization was achieved via grafting with (3-aminopropyl) triethoxysilane with modification from reported procedures.[69] Specifically, 6.3 μL of (3-aminopropyl) triethoxysilane was added into the reaction vessel and allowed to react for 8 h. The final amine-functionalized mesoporous silica-coated UCNPs (UCNP@MSN-NH$_2$) were collected by centrifugation (6000 rpm) and washed with water three times.

4.6.1. Spiropyran-Based Polymer Coating through Atom Transfer Radical Polymerization (ATRP). Synthesis of **UCNP@MSN-Br Initiator:** In a typical reaction, a degassed CH$_2$Cl$_2$ solution (7.5 mL) of Et$_3$N (20 μL) and 2-bromoisobutyryl bromide (15 μL) was added into UCNP@MSN-NH$_2$ (50 mg). The mixture was stirred for 10 h under N$_2$ protection gas under room-temperature conditions. Subsequently, the product was collected by a centrifuge. The product was washed three times with CH$_2$Cl$_2$ (10 mL × 3).

4.6.2. Synthesis of Spiropyran Methacrylate Monomer (SPMA). A CH$_2$Cl$_2$ solution (3 mL) of 0.2 g of 1-(2-hydroxyethyl)-3,3-dimethyl-6-nitrospiro(2*H*-1-benzopyran-2,2-indoline) (SP-OH) and 288 μL of Et$_3$N was kept at 0 °C under N$_2$ protection gas with aluminum foil covering for minimizing light exposure. Another CH$_2$Cl$_2$ solution (1 mL) containing methacryloyl chloride (170 μL) was transferred to the

SP-OH-containing reaction mixture in a dropwise manner within 0.5 h. The final reaction mixture was allowed to react at room temperature for 10 h before solvent evaporation by a rotary evaporator. The product was purified from the residue through silica gel chromatography.

4.6.3. Surface-Initiated ATRP. In a 10 mL round-bottom flask, UCNP@MSN-Br (12.2 mg), SPMA (100 mg), and CuCl (1.2 mg) were put under a N_2 atmosphere. Subsequently, the flask's atmosphere was evacuated and purged with N_2 gas three times to remove residue oxygen gas from the reaction apparatus. A mixture solution of methanol (0.5 mL), THF (3 mL), and HMTETA (7.79 μL) was added into the flask with subsequent freeze−vacuum−pump−thaw cycles to expel oxygen residues from the reaction mixture. The polymerization reaction was performed in N_2 protection gas at 45 °C for 1 day. Another oxygen-free methanol solution (1 mL) of tBA (34.5 μL) was transferred into the reaction mixture to react for 12 h at the same temperature. The reaction was stopped by oxygen exposure.

4.6.4. Hydrolysis of the Poly(t-butyl acrylate) Blocks. The reaction solvent was removed through a rotavapor. The polymer-coated nanoconstructs were redissolved in CH_2Cl_2. Then, a 5-fold molar excess of CF_3COOH was added to induce the hydrolysis. The mixture reacted under room temperature for 12 h. The reaction solvent was removed through centrifugation (7000 rpm, 10 min). The resultant nanoparticle constructs were washed with CH_2Cl_2 and water four times, respectively.

4.6.5. Integrin Receptor Binding RGD Peptide Conjugation. To conjugate the integrin receptor binding RGD sequence, the nanoparticle surface carboxylic groups were conjugated with RGDSC using EDC/NHS coupling. Specifically, the nanoparticles obtained in Section 4.6.4 were dispersed in 5 mL of DPBS to reach a concentration of 0.2 mg/mL. Subsequently, the 5 mL DPBS solution of NHS (1.00 mg) and EDC·HCl (1.67 mg) was mixed with the nanoparticle solution under 4 °C for 30 min and stirred for another 3 h. The resulting mixture was purified by DI water three times and redispersed in DPBS for immediate usage.

4.7. HiPSC-NSCs Culture. Tissue culture vessels were coated with Matrigel (Corning) 1:200 dilution with Dulbecco's modified Eagle's medium (DMEM) (Invitrogen) at 37 °C for 1 h. hiPSC-NSCs were derived from hiPSCs (WT126 clone 8; and WT33 clone 1). iPSC-NSCs proliferated in a growth media containing DMEM/F12 with Glutamax (Thermo Fisher Scientific), B27-supplement w/o Vitamin A (Thermo Fisher Scientific), N2 Supplement (Thermo Fisher Scientific), and 20 ng/mL bFGF (Peprotech). The culture media was changed every other day.

4.8. Cell Viability Characterization. Cell viability assays were conducted in 96-well plates coated with Matrigel (Corning) 1:200 dilution with DMEM (Thermo Fisher Scientific) at 37 °C for 1 h. 20k of human-induced pluripotent stem cell-derived neural stem cells (hiPSC-NSCs) in 100 μL of growth medium were seeded into each well. For nanoparticle concentration-dependent viability, increasing nanoparticle concentrations (0−200 mg/mL) were added into the well plate at day 1 for 24 h incubation. Subsequently, a resazurin-based viability reagent, PrestoBlue, was introduced into each well with 30 min incubation (day 2). Fluorescence intensity was determined through a microplate reader at 590 nm emission with 530 nm excitation. For NIR-intensity-based viability, an increasing 808 nm laser power density (0−8.42 W/cm^2) with irradiation diameter (6 mm) was applied to each well on day 1. The well plates were stored in an incubator for 24 h, followed by PrestoBlue-based viability assay, as described above (day 2).

4.9. 808 nm NIR-Mediated hiPSC-NSCs Differentiation. 808 nm NIR-mediated hiPSC-NSCs differentiation experiments were conducted in 48-well plates, which were coated with Matrigel (Corning) 1:200 dilution with DMEM (Thermo Fisher Scientific) at 37 °C for 1 h. 30k of human-induced pluripotent stem cell-derived neural stem cells (hiPSC-NSCs) in 200 μL of growth medium were seeded into each well. After 24 h with cell attachment on the culture plate, the culture medium was changed to nanoparticle constructs solution [100 μg/mL loaded with 2 μM RA DMSO solution by UV illumination (60 s), nanoparticle constructs mixing, and subsequent green illumination (90 s) for capping]. After 8 h of nanoparticle incubation, an NIR illumination with 1.05 W/cm^2 power density was utilized to trigger the uncapping and release of RA (3 min × 5 min illumination with 5 min interval).

4.10. 3 × 3 hiPSC-NSCs 2D Colony Formation and Culture. *4.10.1. 3 × 3 PDMS Hole Array Fabrication.* A well-mixed PDMS prepolymer (Sylgard 184, A and B in a 15:1 ratio) was transferred into a Petri dish to give a 2 mm thick PDMS layer, followed by curing in an 80 °C oven overnight. Subsequently, the PDMS layer was cut into 15 mm × 15 mm squares. A 3 × 3 hole array was generated using a 3 mm diameter puncher.

4.10.2. 3 × 3 hiPSC-NSCs 2D Colony Formation and Culture. A 12-well cell culture plate was first coated with Matrigel (Corning) dissolved in DMEM/F12 (Thermo Fisher Scientific) (1:200) in an incubator for 1 h. With the aspiration of the coating media, a PDMS 3 × 3 hole array mold (ethanol washed) was placed into the well. An hiPSC-NSC media suspension (1 million/mL) was added into each well (3 μL/hole). The seeded culture plate with PDMS mold was carefully located in the incubator to allow cell attachment for 2 h. The PDMS mold was removed with tweezers. The culture well was filled with 1 mL of culture medium for prolonged culture to form hiPSC-NSCs colony patterns.

4.11. Tissue Phantom Synthesis. A gelatin-based tissue phantom mimicking physiological tissue and in vivo tissue model was constructed following the previous report with modifications.[70] UCNP@MSN-NH_2 Tris-buffer dispersion (3 mL, 0.5 mg/mL) was added with sodium azide and gelatin to achieve a homogeneous solution of 15 mM sodium azide and 10 w/v % gelatin, respectively. Under magnetic stirring, the solution was kept at 50 °C for 30 min to dissolve the gelatin and then kept at 37 °C for 30 min. Hemoglobin (human) and intralipid were added to achieve a concentration of 50 μM and 1 v/v %, and the solution was maintained at 37 °C before molding. To create the molded tissue phantom, the solution was poured into a quartz cuvette for penetration depth characterization.

4.12. Immunohistochemistry. In general, cultured cells were washed twice with DPBS (Thermo Fisher Scientific) and treated in formaldehyde solution (4%) for fixation for 20 min, followed by DPBS wash three times. Subsequently, the cells were permeabilized and blocked for nonspecific binding with blocking buffer containing 0.1% Triton X-100 and 5% normal goat serum (Life Technologies) in PBS for 1 h. To characterize the extent of neuronal differentiation, the cells were fixed, blocked, and stained with a primary mouse antibody against TUJ1 (1:500 dilution, Cell Signaling). Specifically, the fixed samples were incubated for 2.5 h at 4 °C in an antibody dilution buffer (PBS containing 10% NGS) with TUJ1 primary antibody. With three times PBS washing, the cells were incubated for 1 h (RT) in antibody dilution buffer containing Hoechst (3 μg/mL, Life Technologies) and antimouse secondary antibody labeled with Alexa Flour 594 (1:500, Life Technologies). Followed by three times PBS washing, the stained samples were visualized through a Nikon T2500 inverted fluorescence microscope. For mature neuronal markers (MAP2 and Synapsin) characterization, the primary rabbit antibody against MAP2 (Cell Signaling) and Synapsin (EMD Millipore) were used at 1:500 dilution. Subsequently, anti-rabbit secondary antibody Alexa Fluor 488 (1:500, Life Technologies) was utilized to visualize the mature neuronal markers through fluorescence microscopy.

4.13. Gene Expression Analysis. The expression levels of target genes were quantified by quantitative reverse transcription PCR (RT-qPCR) of mRNA extracted from tissue culture. The total RNA, including mRNA of interest, was extracted using TRIzol Reagent (Life Technologies). The total RNA (1 μg) was used as a template for a reverse transcription reaction to generate the first-strand complementary DNA (cDNA) using the Superscript III First-Strand Synthesis System (Life Technologies) according to the manufacturer's protocol. The first-strand cDNA was subsequently used for qPCR reaction with gene-specific primers in the presence of Power SYBR Green PCR Master Mix (Applied Biosystems) on a StepOnePlus Real-Time PCR System (Applied Biosystems). The output C_t values were normalized GAPDH, which is selected as the endogenous control. The standard cycling conditions were applied to all of the reaction conditions with a melting temperature of 60 °C. All gene-specific primers were obtained from the PrimerBank database and are listed in Table S2.

4.14. Calcium Imaging. Differentiated neurons were incubated with 5 μM Fluo-4-AM (Life Technologies) media for 30 min. Subsequently, the treated cells will be washed with HBSS (Life Technologies) and incubated for 30 min in culture media for the deesterification process of the dye. The media was changed to HBSS for the initiation of the calcium imaging session. Under the movie mode of Nikon Eclipse Ti-E microscope, a concentrated KCl solution in PBS (50 mM, 0.1 mL) was introduced into the neuron cultures. The video was captured at a 60 frames per second imaging speed.

ASSOCIATED CONTENT

Supporting Information

The Supporting Information is available free of charge at https://pubs.acs.org/doi/10.1021/acsami.0c10145.

> NIR penetration depth and heating effect, TEM characterization of core−shell UCNPs, luminescence decay of synthesized core−shell UCNPs, TEM characterizations of core−shell UCNP with varied Nd^{3+} and Yb^{3+} concentrations, luminescent spectra of synthesized UCNPs, lattice characterizations and particle distribution analysis of the core−shell structures, composition analysis of the UCNPs synthesized through ICP-OES, photoswitching monomer characterization, FTIR characterization of polymer-functionalized UCNPs, hiPSC-NSCs cellular uptake, cytotoxicity characterizations, proliferation characterizations through microscopy and immunofluorescence staining, hiPSC-NSCs stemness characterizations through immunofluorescence staining, releasing profile under dark conditions, spatial small-molecule release analysis, NIR-based tissue phantom penetration characterization, heating effect comparison, and primer sequences for quantitative PCR (PDF)

AUTHOR INFORMATION

Corresponding Author

Ki-Bum Lee − *Department of Chemistry and Chemical Biology, Rutgers, The State University of New Jersey, Piscataway, New Jersey 08854, United States;* orcid.org/0000-0002-8164-0047; Phone: 1-732-445-2081; Email: kblee@rutgers.edu; Fax: +1-732-445-5312

Authors

Yixiao Zhang − *Department of Chemistry and Chemical Biology, Rutgers, The State University of New Jersey, Piscataway, New Jersey 08854, United States;* orcid.org/0000-0002-3455-7830

Lisa M. Wiesholler − *Institute of Analytical Chemistry, Chemo- and Biosensors, University of Regensburg, 93040 Regensburg, Germany*

Hudifah Rabie − *Department of Chemistry and Chemical Biology, Rutgers, The State University of New Jersey, Piscataway, New Jersey 08854, United States*

Pengfei Jiang − *Department of Chemistry and Chemical Biology, Rutgers, The State University of New Jersey, Piscataway, New Jersey 08854, United States*

Jinping Lai − *Department of Chemistry and Chemical Biology, Rutgers, The State University of New Jersey, Piscataway, New Jersey 08854, United States*

Thomas Hirsch − *Institute of Analytical Chemistry, Chemo- and Biosensors, University of Regensburg, 93040 Regensburg, Germany*

Complete contact information is available at:
https://pubs.acs.org/10.1021/acsami.0c10145

Notes

The authors declare no competing financial interest.

ACKNOWLEDGMENTS

K.-B.L. acknowledges partial financial support from the NIH R21 (1R21NS085569 and R21AR071101), NIH R01 (1R01DC016612-01 and 3R01DC016612-01S1), New Jersey Commission on Spinal Cord Research [CSCR17IRG010 and CSCR16ERG019], NSF [CHE-1429062 and CBET-1803517], and ACS New Directions Award (PRF# 55869-ND10). T.H. acknowledges Sandy Himmelstoß for the TEM studies.

REFERENCES

(1) Sasai, Y. Cytosystems Dynamics in Self-Organization of Tissue Architecture. *Nature* **2013**, *493*, 318.

(2) McGuigan, A. P.; Javaherian, S. Tissue Patterning: Translating Design Principles from in Vivo to in Vitro. *Annu. Rev. Biomed. Eng.* **2016**, *18*, 1−24.

(3) Kinney, M. A.; McDevitt, T. C. Emerging Strategies for Spatiotemporal Control of Stem Cell Fate and Morphogenesis. *Trends Biotechnol.* **2013**, *31*, 78−84.

(4) Gitler, A. D.; Dhillon, P.; Shorter, J. Neurodegenerative Disease: Models, Mechanisms, and a New Hope. *Dis. Models Mech.* **2017**, *10*, 499−502.

(5) Lee, J.-H.; Luo, J.; Choi, H. K.; Chueng, S.-T. D.; Lee, K.-B.; Choi, J.-W. Functional Nanoarrays for Investigating Stem Cell Fate and Function. *Nanoscale* **2020**, 9306−9326.

(6) Rabie, H.; Zhang, Y.; Pasquale, N.; Lagos, M. J.; Batson, P. E.; Lee, K.-B. Nir Biosensing of Neurotransmitters in Stem Cell-Derived Neural Interface Using Advanced Core−Shell Upconversion Nanoparticles. *Adv. Mater.* **2019**, *31*, No. 1806991.

(7) Ming, G.-l.; Song, H. Adult Neurogenesis in the Mammalian Brain: Significant Answers and Significant Questions. *Neuron* **2011**, *70*, 687−702.

(8) Kang, K.; Choi, S.-E.; Jang, H. S.; Cho, W. K.; Nam, Y.; Choi, I. S.; Lee, J. S. In Vitro Developmental Acceleration of Hippocampal Neurons on Nanostructures of Self-Assembled Silica Beads in Filopodium-Size Ranges. *Angew. Chem., Int. Ed.* **2012**, *51*, 2855−2858.

(9) Kang, K.; Park, Y.-S.; Park, M.; Jang, M. J.; Kim, S.-M.; Lee, J.; Choi, J. Y.; Jung, D. H.; Chang, Y.-T.; Yoon, M.-H.; Lee, J. S.; Nam, Y.; Choi, I. S. Axon-First Neuritogenesis on Vertical Nanowires. *Nano Lett.* **2016**, *16*, 675−680.

(10) Park, Y.-S.; Yoon, S. Y.; Park, J. S.; Lee, J. S. Deflection Induced Cellular Focal Adhesion and Anisotropic Growth on Vertically Aligned Silicon Nanowires with Differing Elasticity. *NPG Asia Mater.* **2016**, *8*, e249.

(11) Obernier, K.; Alvarez-Buylla, A. Neural Stem Cells: Origin, Heterogeneity and Regulation in the Adult Mammalian Brain. *Development* **2019**, *146*, No. dev156059.

(12) Guillemot, F. Spatial and Temporal Specification of Neural Fates by Transcription Factor Codes. *Development* **2007**, *134*, 3771−3780.

(13) Kohwi, M.; Doe, C. Q. Temporal Fate Specification and Neural Progenitor Competence During Development. *Nat. Rev. Neurosci.* **2013**, *14*, 823−838.

(14) Cederquist, G. Y.; Asciolla, J. J.; Tchieu, J.; Walsh, R. M.; Cornacchia, D.; Resh, M. D.; Studer, L. Specification of Positional Identity in Forebrain Organoids. *Nat. Biotechnol.* **2019**, 37, 436−444.

(15) Ferreira, L.; Karp, J. M.; Nobre, L.; Langer, R. New Opportunities: The Use of Nanotechnologies to Manipulate and Track Stem Cells. *Cell Stem Cell* **2008**, *3*, 136−146.

(16) Carradori, D.; Eyer, J.; Saulnier, P.; Préat, V.; des Rieux, A. The Therapeutic Contribution of Nanomedicine to Treat Neurodegenerative Diseases Via Neural Stem Cell Differentiation. *Biomaterials* **2017**, *123*, 77−91.

(17) Li, J.; Leung, C. W. T.; Wong, D. S. H.; Xu, J.; Li, R.; Zhao, Y.; Yung, C. Y. Y.; Zhao, E.; Tang, B. Z.; Bian, L. Photocontrolled Sirna Delivery and Biomarker-Triggered Luminogens of Aggregation-Induced Emission by up-Conversion Nayf4:Yb3+Tm3+@Sio2 Nanoparticles for Inducing and Monitoring Stem-Cell Differentiation. *ACS Appl. Mater. Interfaces* **2017**, 22074−22084.

(18) Ma, Y.; Bao, J.; Zhang, Y.; Li, Z.; Zhou, X.; Wan, C.; Huang, L.; Zhao, Y.; Han, G.; Xue, T. Mammalian near-Infrared Image Vision through Injectable and Self-Powered Retinal Nanoantennae. *Cell* **2019**, *177*, 243−255.e15.

(19) Cho, H.-Y.; Hossain, M. K.; Lee, J.-H.; Han, J.; Lee, H. J.; Kim, K.-J.; Kim, J.-H.; Lee, K.-B.; Choi, J.-W. Selective Isolation and Noninvasive Analysis of Circulating Cancer Stem Cells through Raman Imaging. *Biosens. Bioelectron.* **2018**, *102*, 372−382.

(20) Liu, D.; Xu, X.; Wang, F.; Zhou, J.; Mi, C.; Zhang, L.; Lu, Y.; Ma, C.; Goldys, E.; Lin, J.; Jin, D. Emission Stability and Reversibility of Upconversion Nanocrystal. *J. Mater. Chem. C* **2016**, *4*, 9227−9234.

(21) Han, S.; Deng, R.; Xie, X.; Liu, X. Enhancing Luminescence in Lanthanide-Doped Upconversion Nanoparticles. *Angew. Chem., Int. Ed.* **2014**, *53*, 11702−11715.

(22) Lin, X.; Chen, X.; Zhang, W.; Sun, T.; Fang, P.; Liao, Q.; Chen, X.; He, J.; Liu, M.; Wang, F.; Shi, P. Core−Shell−Shell Upconversion Nanoparticles with Enhanced Emission for Wireless Optogenetic Inhibition. *Nano Lett.* **2018**, *18*, 948−956.

(23) Liu, Y.; Lu, Y.; Yang, X.; Zheng, X.; Wen, S.; Wang, F.; Vidal, X.; Zhao, J.; Liu, D.; Zhou, Z.; Ma, C.; Zhou, J.; Piper, J. A.; Xi, P.; Jin, D. Amplified Stimulated Emission in Upconversion Nanoparticles for Super-Resolution Nanoscopy. *Nature* **2017**, *543*, 229−233.

(24) Zhu, X.; Li, J.; Qiu, X.; Liu, Y.; Feng, W.; Li, F. Upconversion Nanocomposite for Programming Combination Cancer Therapy by Precise Control of Microscopic Temperature. *Nat. Commun.* **2018**, *9*, No. 2176.

(25) Hou, Z.; Deng, K.; Wang, M.; Liu, Y.; Chang, M.; Huang, S.; Li, C.; Wei, Y.; Cheng, Z.; Han, G.; Al Kheraif, A. A.; Lin, J. Hydrogenated Titanium Oxide Decorated Upconversion Nanoparticles: Facile Laser Modified Synthesis and 808 Nm near-Infrared Light Triggered Phototherapy. *Chem. Mater.* **2019**, *31*, 774−784.

(26) Idris, N. M.; Gnanasammandhan, M. K.; Zhang, J.; Ho, P. C.; Mahendran, R.; Zhang, Y. In Vivo Photodynamic Therapy Using Upconversion Nanoparticles as Remote-Controlled Nanotransducers. *Nat. Med.* **2012**, *18*, 1580−1585.

(27) Ai, X.; Ho, C. J. H.; Aw, J.; Attia, A. B. E.; Mu, J.; Wang, Y.; Wang, X.; Wang, Y.; Liu, X.; Chen, H.; Gao, M.; Chen, X.; Yeow, E. K. L.; Liu, G.; Olivo, M.; Xing, B. In Vivo Covalent Cross-Linking of Photon-Converted Rare-Earth Nanostructures for Tumour Localization and Theranostics. *Nat. Commun.* **2016**, *7*, No. 10432.

(28) He, L.; Zhang, Y.; Ma, G.; Tan, P.; Li, Z.; Zang, S.; Wu, X.; Jing, J.; Fang, S.; Zhou, L.; Wang, Y.; Huang, Y.; Hogan, P. G.; Han, G.; Zhou, Y. Near-Infrared Photoactivatable Control of Ca2+ Signaling and Optogenetic Immunomodulation. *eLife* **2015**, *4*, No. e10024.

(29) Liu, J.; Bu, W.; Pan, L.; Shi, J. Nir-Triggered Anticancer Drug Delivery by Upconverting Nanoparticles with Integrated Azobenzene-Modified Mesoporous Silica. *Angew. Chem., Int. Ed.* **2013**, *52*, 4375−4379.

(30) Lai, J.; Shah, B. P.; Zhang, Y.; Yang, L.; Lee, K.-B. Real-Time Monitoring of Atp-Responsive Drug Release Using Mesoporous-Silica-Coated Multicolor Upconversion Nanoparticles. *ACS Nano* **2015**, *9*, 5234−5245.

(31) Liu, C.; Zhang, Y.; Liu, M.; Chen, Z.; Lin, Y.; Li, W.; Cao, F.; Liu, Z.; Ren, J.; Qu, X. A Nir-Controlled Cage Mimicking System for Hydrophobic Drug Mediated Cancer Therapy. *Biomaterials* **2017**, *139*, 151−162.

(32) Min, Y.; Li, J.; Liu, F.; Yeow, E. K. L.; Xing, B. Near-Infrared Light-Mediated Photoactivation of a Platinum Antitumor Prodrug and Simultaneous Cellular Apoptosis Imaging by Upconversion-Luminescent Nanoparticles. *Angew. Chem., Int. Ed.* **2014**, *53*, 1012−1016.

(33) Chen, S.; Weitemier, A. Z.; Zeng, X.; He, L.; Wang, X.; Tao, Y.; Huang, A. J. Y.; Hashimotodani, Y.; Kano, M.; Iwasaki, H.; Parajuli, L. K.; Okabe, S.; Teh, D. B. L.; All, A. H.; Tsutsui-Kimura, I.; Tanaka, K. F.; Liu, X.; McHugh, T. J. Near-Infrared Deep Brain Stimulation Via Upconversion Nanoparticle−Mediated Optogenetics. *Science* **2018**, *359*, 679−684.

(34) All, A. H.; Zeng, X.; Teh, D. B. L.; Yi, Z.; Prasad, A.; Ishizuka, T.; Thakor, N.; Hiromu, Y.; Liu, X. Expanding the Toolbox of Upconversion Nanoparticles for in Vivo Optogenetics and Neuromodulation. *Adv. Mater.* **2019**, *31*, No. 1803474.

(35) Ai, X.; Lyu, L.; Zhang, Y.; Tang, Y.; Mu, J.; Liu, F.; Zhou, Y.; Zuo, Z.; Liu, G.; Xing, B. Remote Regulation of Membrane Channel Activity by Site-Specific Localization of Lanthanide-Doped Upconversion Nanocrystals. *Angew. Chem., Int. Ed.* **2017**, *56*, 3031−3035.

(36) Zhang, Y.; Zheng, F.; Yang, T.; Zhou, W.; Liu, Y.; Man, N.; Zhang, L.; Jin, N.; Dou, Q.; Zhang, Y.; Li, Z.; Wen, L.-P. Tuning the Autophagy-Inducing Activity of Lanthanide-Based Nanocrystals through Specific surface-Coating Peptides. *Nat. Mater.* **2012**, *11*, 817−826.

(37) Liu, M.; Shu, M.; Xu, W.; Liu, X.; Hou, Z.; Xing, B.; Lin, J. Bmp-2-Loaded Hap:Ln3+ (Ln = Yb, Er, Gd) Nanorods with Dual-Mode Imaging for Efficient Mc3t3-E1 Cell Differentiation Regulation. *Langmuir* **2019**, *35*, 15287−15294.

(38) Kang, H.; Zhang, K.; Wong, D. S. H.; Han, F.; Li, B.; Bian, L. Near-Infrared Light-Controlled Regulation of Intracellular Calcium to Modulate Macrophage Polarization. *Biomaterials* **2018**, *178*, 681−696.

(39) Yan, Z.; Qin, H.; Ren, J.; Qu, X. Photocontrolled Multidirectional Differentiation of Mesenchymal Stem Cells on an Upconversion Substrate. *Angew. Chem., Int. Ed.* **2018**, *57*, 11182−11187.

(40) Kang, H.; Zhang, K.; Pan, Q.; Lin, S.; Wong, D. S. H.; Li, J.; Lee, W. Y.-W.; Yang, B.; Han, F.; Li, G.; Li, B.; Bian, L. Remote Control of Intracellular Calcium Using Upconversion Nanotransducers Regulates Stem Cell Differentiation in Vivo. *Adv. Funct. Mater.* **2018**, *28*, No. 1802642.

(41) Xie, X.; Gao, N.; Deng, R.; Sun, Q.; Xu, Q.-H.; Liu, X. Mechanistic Investigation of Photon Upconversion in Nd3+-Sensitized Core−Shell Nanoparticles. *J. Am. Chem. Soc.* **2013**, *135*, 12608−12611.

(42) Vetrone, F.; Naccache, R.; Mahalingam, V.; Morgan, C. G.; Capobianco, J. A. The Active-Core/Active-Shell Approach: A Strategy to Enhance the Upconversion Luminescence in Lanthanide-Doped Nanoparticles. *Adv. Funct. Mater.* **2009**, *19*, 2924−2929.

(43) Tuchinda, C.; Lim, H. W.; Strickland, F. M.; Guzmán, E. A.; Wong, H. K. Comparison of Broadband Uvb, Narrowband Uvb, Broadband Uva and Uva1 on Activation of Apoptotic Pathways in Human Peripheral Blood Mononuclear Cells. *Photodermatol., Photoimmunol. Photomed.* **2007**, *23*, 2−9.

(44) Place, E. S.; Evans, N. D.; Stevens, M. M. Complexity in Biomaterials for Tissue Engineering. *Nat. Mater.* **2009**, *8*, 457−470.

(45) Fan, W.; Huang, P.; Chen, X. Overcoming the Achilles' Heel of Photodynamic Therapy. *Chem. Soc. Rev.* **2016**, *45*, 6488−6519.

(46) Liu, B.; Li, C.; Yang, P.; Hou, Z.; Lin, J. 808-Nm-Light-Excited Lanthanide-Doped Nanoparticles: Rational Design, Luminescence Control and Theranostic Applications. *Adv. Mater.* **2017**, *29*, No. 1605434.

(47) Bei, L.; Chunxia, L.; Piaoping, Y.; Zhiyao, H.; Jun, L. 808-Nm-Light-Excited Lanthanide-Doped Nanoparticles: Rational Design, Luminescence Control and Theranostic Applications. *Adv. Mater.* **2017**, *29*, No. 1605434.

(48) Wiesholler, L. M.; Hirsch, T. Strategies for the Design of Bright Upconversion Nanoparticles for Bioanalytical Applications. *Opt. Mater.* **2018**, *80*, 253−264.

(49) Arboleda, C.; He, S.; Stubelius, A.; Johnson, N. J. J.; Almutairi, A. High Nd(Iii)-Sensitizer Concentrations for 800 Nm Wavelength Excitation Using Isotropic Core−Shell Upconversion Nanoparticles. *Chem. Mater.* **2019**, *31*, 3103−3110.

(50) Yu, Z.; Chan, W. K.; Tan, T. T. Y. Neodymium-Sensitized Nanoconstructs for near-Infrared Enabled Photomedicine. *Small* **2020**, *16*, No. 1905265.

(51) Dai, Y.; Bi, H.; Deng, X.; Li, C.; He, F.; Ma, Pa.; Yang, P.; Lin, J. 808 Nm near-Infrared Light Controlled Dual-Drug Release and Cancer Therapy in Vivo by Upconversion Mesoporous Silica Nanostructures. *J. Mater. Chem. B* **2017**, *5*, 2086−2095.

(52) Zhang, Y.; Yu, Z.; Li, J.; Ao, Y.; Xue, J.; Zeng, Z.; Yang, X.; Tan, T. T. Y. Ultrasmall-Superbright Neodymium-Upconversion Nanoparticles Via Energy Migration Manipulation and Lattice Modification: 808 Nm-Activated Drug Release. *ACS Nano* **2017**, *11*, 2846−2857.

(53) Zhao, T.; Wang, P.; Li, Q.; Al-Khalaf, A. A.; Hozzein, W. N.; Zhang, F.; Li, X.; Zhao, D. Near-Infrared Triggered Decomposition of Nanocapsules with High Tumor Accumulation and Stimuli Responsive Fast Elimination. *Angew. Chem., Int. Ed.* **2018**, *57*, 2611−2615.

(54) Duester, G. Retinoic Acid Synthesis and Signaling During Early Organogenesis. *Cell* **2008**, *134*, 921−931.

(55) Mohammadniaei, M.; Yoon, J.; Choi, H. K.; Placide, V.; Bharate, B. G.; Lee, T.; Choi, J.-W. Multifunctional Nanobiohybrid Material Composed of Ag@Bi2se3/Rna Three-Way Junction/Mirna/Retinoic Acid for Neuroblastoma Differentiation. *ACS Appl. Mater. Interfaces* **2019**, *11*, 8779−8788.

(56) Wang, F.; Deng, R.; Wang, J.; Wang, Q.; Han, Y.; Zhu, H.; Chen, X.; Liu, X. Tuning Upconversion through Energy Migration in Core−Shell Nanoparticles. *Nat. Mater.* **2011**, *10*, 968−973.

(57) Hynes, R. O. Integrins: Bidirectional, Allosteric Signaling Machines. *Cell* **2002**, *110*, 673−687.

(58) Wang, H.; Luo, X.; Leighton, J. Extracellular Matrix and Integrins in Embryonic Stem Cell Differentiation. *Biochem. Insights* **2015**, *8s2*, No. BCI.S30377.

(59) Li, Y.; Liu, M.; Yan, Y.; Yang, S.-T. Neural Differentiation from Pluripotent Stem Cells: The Role of Natural and Synthetic Extracellular Matrix. *World J. Stem Cells* **2014**, *6*, 11−23.

(60) Kulangara, K.; Adler, A. F.; Wang, H.; Chellappan, M.; Hammett, E.; Yasuda, R.; Leong, K. W. The Effect of Substrate Topography on Direct Reprogramming of Fibroblasts to Induced Neurons. *Biomaterials* **2014**, *35*, 5327−5336.

(61) Perez, R. A.; Choi, S.-J.; Han, C.-M.; Kim, J.-J.; Shim, H.; Leong, K. W.; Kim, H.-W. Biomaterials Control of Pluripotent Stem Cell Fate for Regenerative Therapy. *Prog. Mater. Sci.* **2016**, *82*, 234−293.

(62) Clarke, K. E.; Tams, D. M.; Henderson, A. P.; Roger, M. F.; Whiting, A.; Przyborski, S. A. A Robust and Reproducible Human Pluripotent Stem Cell Derived Model of Neurite Outgrowth in a Three-Dimensional Culture System and Its Application to Study Neurite Inhibition. *Neurochem. Int.* **2017**, *106*, 74−84.

(63) Korzhevskii, D. E.; Karpenko, M. N.; Kirik, O. V. Microtubule-Associated Proteins as Indicators of Differentiation and the Functional State of Nerve Cells. *Neurosci. Behav. Physiol.* **2012**, *42*, 215−222.

(64) Cesca, F.; Baldelli, P.; Valtorta, F.; Benfenati, F. The Synapsins: Key Actors of Synapse Function and Plasticity. *Prog. Neurobiol.* **2010**, *91*, 313−348.

(65) Patel, S.; Chueng, S.-T. D.; Yin, P. T.; Dardir, K.; Song, Z.; Pasquale, N.; Kwan, K.; Sugiyama, H.; Lee, K.-B. Induction of Stem-Cell-Derived Functional Neurons by Nanoscript-Based Gene Repression. *Angew. Chem., Int. Ed.* **2015**, *54*, 11983−11988.

(66) Wang, M.; Xu, Z.; Liu, Q.; Sun, W.; Jiang, B.; Yang, K.; Li, J.; Gong, Y.; Liu, Q.; Liu, D.; Li, X. Nongenetic Optical Modulation of Neural Stem Cell Proliferation and Neuronal/Glial Differentiation. *Biomaterials* **2019**, *225*, No. 119539.

(67) Wilhelm, S.; Kaiser, M.; Würth, C.; Heiland, J.; Carrillo-Carrion, C.; Muhr, V.; Wolfbeis, O. S.; Parak, W. J.; Resch-Genger, U.; Hirsch, T. Water Dispersible Upconverting Nanoparticles: Effects of Surface Modification on Their Luminescence and Colloidal Stability. *Nanoscale* **2015**, *7*, 1403−1410.

(68) Wilhelm, S.; del Barrio, M.; Heiland, J.; Himmelstoß, S. F.; Galbán, J.; Wolfbeis, O. S.; Hirsch, T. Spectrally Matched Upconverting Luminescent Nanoparticles for Monitoring Enzymatic Reactions. *ACS Appl. Mater. Interfaces* **2014**, *6*, 15427−15433.

(69) Sándor, M.; Nistor, C. L.; Szalontai, G.; Stoica, R.; Nicolae, C. A.; Alexandrescu, E.; Fazakas, J.; Oancea, F.; Donescu, D. Aminopropyl-Silica Hybrid Particles as Supports for Humic Acids Immobilization. *Materials* **2016**, *9*, No. 34.

(70) Zhu, X.; Feng, W.; Chang, J.; Tan, Y.-W.; Li, J.; Chen, M.; Sun, Y.; Li, F. Temperature-Feedback Upconversion Nanocomposite for Accurate Photothermal Therapy at Facile Temperature. *Nat. Commun.* **2016**, *7*, No. 10437.